Designing Multiscale Porous Metal by Simple Dealloying with 3D Morphological Evolution Mechanism Revealed via X-ray Nano-tomography

Lijie Zou,[†,‡] Mingyuan Ge,[§] Chonghang Zhao,[‡] Qingkun Meng,[∥,‡] Hao Wang,[†] Xiaoyang Liu,[‡] Cheng-Hung Lin,[‡] Xianghui Xiao,[§] Wah-Keat Lee,[§] Qiang Shen,*[,†] Fei Chen,*[,†] and Yu-chen Karen Chen-Wiegart*[,‡,§]

[†]State Key Lab of Advanced Technology for Materials Synthesis and Processing, Wuhan University of Technology, Wuhan 430070, China
[‡]Department of Materials Science and Chemical Engineering, Stony Brook University, Stony Brook, New York 11794, United States
[§]National Synchrotron Light Source - II, Brookhaven National Laboratory, Upton, New York 11973, United States
[∥]School of Materials Science and Engineering, China University of Mining and Technology, Xuzhou 221116, China

Ⓢ Supporting Information

ABSTRACT: Designing materials with multiscale, hierarchical structure is critical to drive the advancement of new technology. Specifically, porous metals with multiscale porosity from nanometer to micrometer sizes would lead to enhanced physical and chemical properties—the micron-sized pores can increase the effective diffusivity of ion transport within the porous media, and the nano-sized pores provide high specific surface area, enabling functionalities that are unique to nanoporous metals. A new ternary precursor alloy selection concept utilizing the different mixing enthalpies is demonstrated in this work for the design of multiscale, bimodal porous copper from a simple, one-step dealloying of Cu−Fe−Al ternary alloy. The nanoporosity in the bimodal porous structure is formed from dealloying of the Cu-rich phase, whereas the microporosity is controlled by dissolving the Fe-rich phase, determined by both the initial Fe particle size and sintering profile. In addition to advancing the materials design method, the multiscale pore formation during dealloying was directly visualized and quantified via an interrupted in situ synchrotron X-ray nano-tomography. The 3D morphological analysis on tortuosity showed that the presence of the microporosity can compensate the increase of the diffusion path length due to nanoporosity, which facilitates diffusion within the porous structure. Overall the focus of the work is to introduce a new strategy to design multiscale porous metals with enhanced transport properties, and sheds light on the fundamental mechanisms on the 3D morphological evolution of the system using advanced synchrotron X-ray nano-tomography for future materials development and applications.

KEYWORDS: bimodal porous Cu, materials design, 3D morphology, nano-CT, TXM
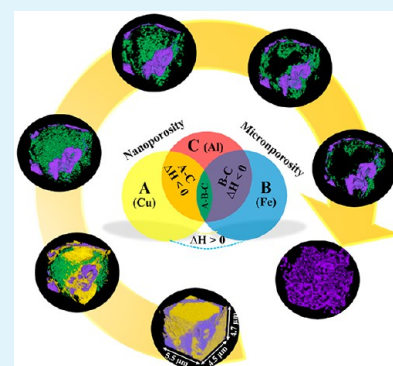
1. INTRODUCTION

Porous metals as a unique class of materials possess notable characteristics including low relative density, high specific surface area, high specific strength, and high permeability, which leads to a wide range of applications, including batteries,[1−4] electrochemical sensors,[5] catalysts,[6,7] fuel cells,[8] filters,[9] heat exchangers,[10] sound absorbers,[11] and mechanical actuators.[12] Porous metals with a pore size ranging from the nanometer scale to micrometer scale can be fabricated by various methods, such as electrochemical deposition, templating and dealloying.[13,7,14,15] Specifically, dealloying has attracted great attention for fabricating three-dimensional (3D) bicontinuous nanoporous metals via a selective dissolution and self-rearrangement mechanism. While presenting excellent functional properties on the surface, nanoporous structure may exhibit limitation in its transport properties owing to its

tortuous diffusion path. To enhance the transport properties of porous material, a multiscale porous structure which has both the nano-sized and micron-sized pores would offer unique properties. A recent review highlights the advances of new research areas in using nanoporous metals as a base structure while incorporating structural hierarchy for novel properties or applications such as catalysis and electrochemistry.[16] Such bimodal property is particularly beneficial for functional materials which involve mass transport applications.[17−20] Nanopores can increase the specific surface area (surface area per unit volume) for enhanced chemical or electrochemical reactions and micropores can facilitate the transport
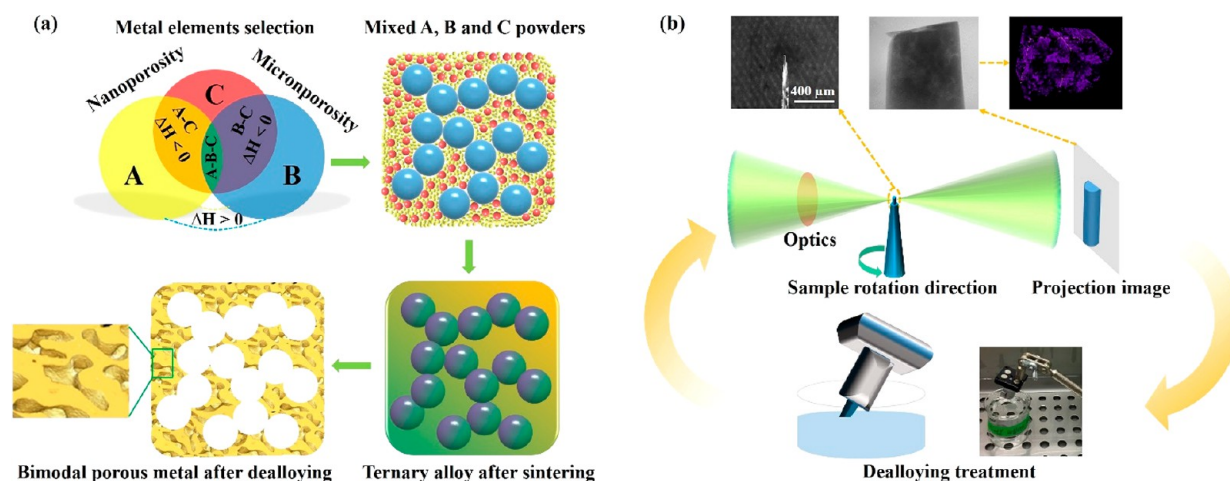
Figure 1. (a) Design concept of bimodal porous metal fabricated by a simple one-step dealloying of ternary alloys; any B-rich phase (B−C (−A) phase) no matter containing C or C−A can be dissolved to form micron-sized pores where the size is controlled by both the initial particle size of B and sintering profile, whereas any A-rich phase (A−C (−B) phase) no matter containing C or C−B can be dealloyed to form a percolated nanoporous A. (b) Experimental setup and interrupted in situ dealloying treatment for synchrotron transmission X-ray microscopy characterization. The dealloying process was conducted in a 5 wt % sulfuric acid solution at both 90 and 60 °C separately to study the temperature dependence of porous structure.

of ions over the long-range diffusion into the materials[21] by reducing the tortuosity of the materials, thereby increasing its effective diffusivity.[21−23]

To-date, five main techniques involving the dealloying method have been demonstrated to fabricate multiscale porous metals: a two-step dealloying method,[24] templating combined with the dealloying method,[25] dealloying of intermetallic and metallic elemental phases method,[26] a ternary alloy dealloying method[27] and direct printing combined with the dealloying method.[28,29] As novel methods, these methods used to fabricate multiscale porous metal mentioned possess different challenges. The technology of the two-step dealloying method, direct printing combined with dealloying method and template combined with dealloying method, involve multistep processing procedures. The dealloying of intermetallic and metallic elemental phases method applies to a rather narrow composition range of precursor alloys, which will limit the achievable range of micro- and nanoporosity. Ternary alloy dealloying has been demonstrated in prior studies to enable additional structural, morphological, and chemical tuning of nanoporous metal design, such as stabilizing nanoporous gold coarsening by introducing Pt.[27] However, it is challenging to obtain pure bimodal porous metals.

As the focus of this work, we demonstrated a new approach to fabricate bimodal porous metal with controllable microporosity via a simple, one-step dealloying method of a ternary alloy. The concept involves choosing an alloy system A−B−C formed by powder metallurgy with micron-sized powders, where both B and C are active components, the mixing enthalpy between A and B is positive, and the mixing enthalpy values of the other two binary subsystems A−C and B−C are negative,[30,31] so that A−C (−B) (which means A−C or A−C−B) and B−C (−A) (which means B−C or B−C−A) phases are formed. In a simple treatment step, the B-rich phase can be dissolved to form micron-sized pores where the size is controlled by both the initial particle size of B and sintering profile, whereas the alloy A−C (−B) can be dealloyed to form a percolated nanoporous A. This concept is illustrated below in Figure 1a.

We demonstrated this new method by fabricating multiscale, bimodal porous Cu material, a versatile material with excellent properties and a range of applications[32−36] (further information in the Supporting Information), from dealloying Cu−Fe−Al ternary alloy; following the design concept as outlined above, in which element A is Cu, B is Fe, and C is Al. The mixing enthalpy of Cu−Fe is 13 kJ/mol, for which they are immiscible, whereas the mixing enthalpy for Cu−Al is −1 kJ/mol and Fe−Al is −11 kJ/mol; both are miscible.[30] Here, the role of Al is to alloy with Cu and form a Cu-rich (Cu−Al (−Fe)) phase, so that after the dissolution of active components in the Cu−Al (−Fe) phase, Cu will rearrange and form a nanoporous structure. With the immiscibility with Cu, the role of Fe is to remain its phase separation from the Cu−Al phase and this Fe-rich phase will form a microporous structure upon the dealloying-dissolution process. In addition to innovating a new processing method, we conducted studies on the 3D morphological evolution and phase transformation during the dealloying, by applying advanced synchrotron X-ray nano-tomography (further details in the Supporting Information). An interrupted in situ approach was taken here, in which the same sample was measured and treated repetitively to study the morphological evolution from the same location as the result of the dealloying process.[37−40] Therefore, overall the novelty of this work is 2-fold: one on the demonstration of this new strategy to fabricate bimodal porous metal and one on the use of novel synchrotron X-ray nano-tomography to understand the morphological evolution during the dealloying process. By revealing the underlying dealloying process through studying the temporal evolution of the materials' morphology in this new material processing strategy, the ultimate goal is to be able to precisely control the 3D morphology of the bimodal porous metal to enable novel multiscale materials design for tailored properties and applications.

2. METHODS

2.1. Fabrication of Bimodal Porous Cu. Metal powders of pure Cu (particle size: 1 μm), Fe (particle size: 8 μm), and Al (particle size: 2 μm) purchased from Alfa Aesar (Company, U.S.A.) were used

to prepare $Al_{30}Fe_{45}Cu_{25}$ precursor alloys by plasma activated sintering (PAS) facility (ED-PAS 111, Japan) sintered at 800 °C for 5 min with a heating rate of 50 °C/min. The sintering pressure was 50 MPa, and the vacuum pressure was lower than 10 Pa during the sintering experiments. The sintering process, conducted at a temperature lower than the melting point of pure Cu (1085 °C) and pure Fe (1538 °C), allowed the microstructures of prepared $Al_{30}Fe_{45}Cu_{25}$ precursor alloy to remain a similar length-scale of the initial metal powders upon alloying. In the process, the micron-sized Fe powders formed a micron-sized Fe-rich phase to allow the following dissolution process; a Cu-rich phase was also formed to allow a dealloying process. The characterization of the pristine precursor alloy is presented in the Results and Discussion section. The bimodal porous structure was fabricated by chemical dealloying of the $Al_{30}Fe_{45}Cu_{25}$ precursor alloys using 5 wt % sulfuric acid (H_2SO_4) aqueous solution at 90 and 60 °C. Deionized water was used to prepare the H_2SO_4 solution. The dealloying process finished when no gas bubbles from hydrogen gas evolution emerged in the solution; the dealloying samples were immersed in deionized water and then ethanol for about 20 min consecutively.

The phase composition and surface microstructure of the ternary precursor alloys and porous Cu were investigated through X-ray diffraction (XRD) and scanning electron microscopy (SEM) respectively. In order to observe the morphological evolution of $Al_{30}Fe_{45}Cu_{25}$ alloy, four bulk alloy samples after being dealloyed for different amounts of time were prepared, for the cross-section FIB-SEM analysis. In addition, one $Al_{30}Fe_{45}Cu_{25}$ bulk alloy sample was repeatedly analyzed by alternating dealloying and surface energy dispersive spectroscopy (EDS) measurement, to investigate the chemical composition evolution during interrupted in situ dealloying process. The XRD, SEM, and EDS analysis were conducted at the Center for Functional Nanomaterials (CFN) at Brookhaven National Laboratory (BNL).

2.2. Sample Preparation for X-ray Nano-tomography Characterization.
All samples measured in X-ray nano-tomography characterization were prepared by focused ion beam (FIB) milling at the CFN of BNL. Two samples were imaged as prepared: precursor $Al_{30}Fe_{45}Cu_{25}$ bulk alloy and fully dealloyed porous Cu samples (dealloyed for 24 h at 90 °C) micropillars were milled from selected regions, lifted out, and attached onto a sharp W pin by Pt deposition; the final cylinders were 20−30 μm in diameter and ~50 μm in length following an established procedure published previously.[41] The procedure is shown in the Supporting Information, Figure S3. The interrupted in situ X-ray nano-tomography process involves alternating X-ray nanoimaging at the TXM and dealloying of the same sample repeatedly. Therefore, the standard FIB lift-out process as described previously is not suited for ex situ tomography, as the Pt deposited to attach the sample onto the pin might be mechanically unstable during the repeated treatment process; using a FIB-lift-out sample might lead to sample loss during the experiment. To mitigate this issue, the samples for interrupted in situ X-ray tomography characterization were prepared using a different method demonstrated previously in solid oxide fuel cells studies:[42] $Fe_{75}Cu_{25}$ and $Al_{30}Fe_{45}Cu_{25}$ precursor bulk alloys were first cut by diamond saw into thin strips with the dimension of 10 mm in length and 1 mm in thickness (the thickness is uniform for the whole strips), with the width of the top portion of the thin strips (~0.5 mm) being narrower than the bottom portion. Then the top portion of the thin strips was further polished down to ~0.5 mm, which is the same as the width of top portion. The sharpened tip of the wedge-shaped strips is required to conduct the FIB milling within a reasonable time. The top portion of wedge-shape strips was then milled into micropillars with about 20 μm in diameter and 50 μm in length using a 21 nA ion beam current. The surface of the micropillar was cleaned by 2.8 nA ion beam current to 18 μm in diameter. With this method, the long strips with milled tip can be directly mounted as X-ray nano-tomography samples thus avoiding any binders, glues, or other mechanically unstable methods.

2.3. Synchrotron Transmission X-ray Microscopy Characterization.
Synchrotron X-ray nano-tomography characterization was conducted at full-field X-ray imaging (FXI) Beamline 18-ID, National Synchrotron Light Source II (NSLS-II), Brookhaven National Laboratory. The outstanding capability of the full field transmission X-ray microscopy (TXM) at FXI beamline is the one-minute acquisition time for a full 3D nano-tomography data set with sub-50 nm spatial resolution.[45] Therefore, FXI beamline focuses on high speed imaging for tracking sample dynamics. The TXM utilizes a capillary condenser and a 30 nm outermost Fresnel zone plate as an objective lens. The detector is the Andor Neo 5.5 camera with 2560 (H) × 2160 (V) pixels and 6.5 μm × 6.5 μm pixel size. A total of 1080 projection images (2 × 2 binned) were recorded from 0 to 180° in fly scan mode with a rotation speed of 2 deg/s and an exposure time of 0.015 s. For the parameters used to conduct this work, the field view of the TXM was set to 43 μm × 36 μm, with a pixel size of 34 nm; incident X-ray energy used to collect the tomography was at the above and below Cu K-edge as well as Fe K-edge at 9.1 (above Cu K-edge), 8.95 (below Cu K-edge), 7.2 (above Fe K-edge), and 7.1 (below Fe K-edge) keV, respectively.

In order to study the effect of dealloying temperature on bimodal porous structure, we conducted ex situ measurement of $Al_{30}Fe_{45}Cu_{25}$ alloys dealloyed at both 60 and 90 °C. $Al_{30}Fe_{45}Cu_{25}$ alloy dealloyed at 60 °C was studied at six dealloying time points, 0 (pristine), 10, 30, 40, 50, and 65 min, and $Al_{30}Fe_{45}Cu_{25}$ alloys dealloyed at 90 °C were studied at three dealloying time points, 0 (pristine), 2.5, and 7 min. While, using an "interrupted in situ" has a significant advantage over the conventional method of measuring different samples, which would likely introduce sample/statistical variations as well as the challenges to identify the evolution of specific features continuously. The interrupted in situ X-ray tomography characterization[43,44] was conducted by collecting tomography data of alloys at different dealloying durations; the same samples were measured from the pristine state and different dealloyed states repeatedly via alternating the dealloying and X-ray imaging. The measurement was initially tested at both 60 and 90 °C; the dealloying rate at 60 °C is slower, so that the dealloying process can be better controlled and analyzed quantitatively during the interrupted in situ experiment with X-ray nano-tomography. Therefore, the morphological evolution of bimodal porous Cu dealloyed at 60 °C is the focus of the X-ray nano-tomography analysis. Moreover, $Fe_{75}Cu_{25}$ binary alloy was also studied by interrupted in situ measurement and dealloyed at 90 °C with three dealloying time points, 0 (pristine), 2.5, and 7 min, in order to compare the different dealloying mechanism between $Fe_{75}Cu_{25}$ binary alloy and $Al_{30}Fe_{45}Cu_{25}$ ternary alloy.

2.4. Data Processing and Analyzation.
A filtered back projection (FBP) algorithm was applied to reconstruct the 3D structure from the X-ray nano-tomography characterization data set using the "Gridrec" implementation in Tomopy.[46] Median filter smoothing with kernel size 3 × 3 × 3 was performed in the reconstructed image by replacing each pixel with the median of the neighboring pixel values to reduce the level of noise. Segmentation was applied on the reconstructed images using Trainable Weka Segmentation[47,48] in freeware ImageJ to segment four different phases: pores, ligament, Cu-rich phase and Fe-rich phase. The 3D segmented image stacks were cropped along height direction of cylindrical sample for further analysis. Visualization of 2D pseudo cross-section and 3D morphological evolution was conducted using commercial software Avizo (v.9.3 FEI). Feature size distribution and tortuosity in three dimensions was quantified according to the segmented 3D images and customized Matlab code developed in-house by implementing well-established methods;[49] the feature size for different phases were quantified including the size distribution of pores, ligaments and Cu-rich phase; the algorithm for tortuosity calculation used the "quasi-Euclidean" voxel neighboring definitions.[22] The volume fraction of the 3D structure feature was determined by voxel counting in the image histogram, where the voxel count of one feature was divided by the overall sample volume in voxel numbers. Note that the 3D morphological parameters from the sample with 40 and 50 min of dealloying were not measured, because the tomographic images of these two time points appear to be not in-focus; visualization could still be conducted on these two data sets but not quantitative calculation.
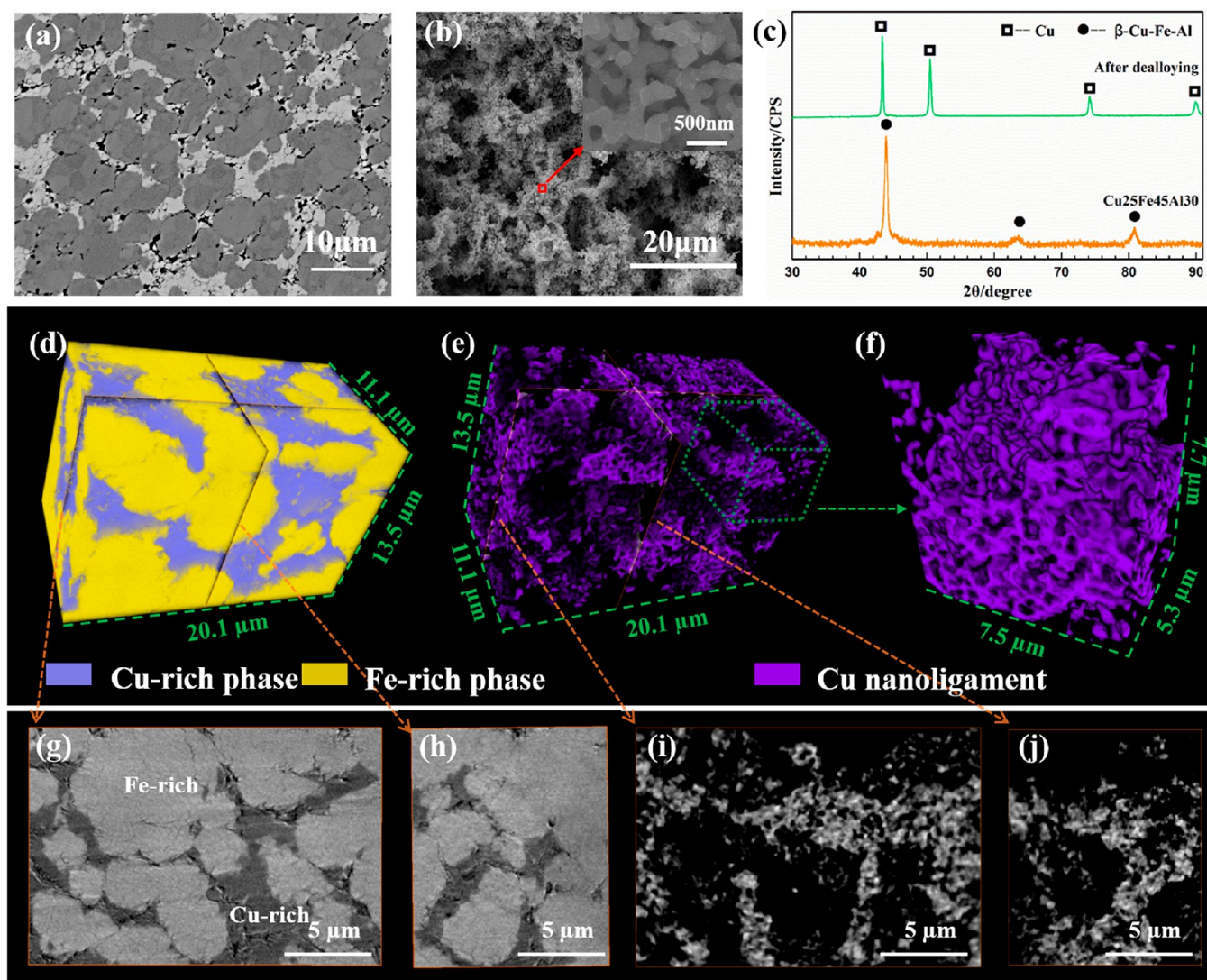
Figure 2. Microstructure, phase composition and 3D morphology of $Al_{30}Fe_{45}Cu_{25}$ precursor alloy and its corresponding fully dealloyed, bimodal porous Cu from dealloying the precursor alloy in 5 wt % H_2SO_4 aqueous solution at 90 °C. SEM images showing surface microstructure of (a) $Al_{30}Fe_{45}Cu_{25}$ alloy precursor and (b) corresponding bimodal porous. (c) XRD diffraction pattern. X-ray nano-tomography reconstruction showing the 3D morphology: (d) $Al_{30}Fe_{45}Cu_{25}$ alloy, (e) bimodal porous Cu with micron- and nano-sized porous; a zoom-in view of the nanoporous structure is shown in (f). Pseudo cross-section images from X-ray nano-tomography for both (g-h) the pristine and (i-j) bimodal porous Cu, imagined at above Cu K-edge, where the X-ray attenuation of the Cu-rich phase is significantly increased, so that the contrast between the Fe-rich and Cu-rich phases can be enhanced.

3. RESULTS AND DISCUSSION

3.1. Morphology of Precursor Alloys and Bimodal Porous Cu.
The microstructure and phase composition of the Cu−Fe−Al ternary alloy and its corresponding multiscale porous Cu are first discussed below. The morphology and phase composition of the precursor alloys, which can influence the final microstructure and homogeneity of porous Cu, as well as the dealloyed bimodal porous Cu, are shown in Figure 2. In this system, because Cu and Fe are highly immiscible, two separate Fe-rich and Cu-rich phases will form after sintering as also demonstrated in our prior work.[50] The particle size of Fe impacts the size of Fe-rich phase directly, and as a result, it also determines the size of micropores in bimodal porous structure. The introduction of Al changes the phase composition of the precursor alloy; the corresponding porous Cu dealloyed from the Cu−Fe−Al alloy thus will have a significantly different morphology from the micron-sized porous Cu formed by

dealloying Cu−Fe. Two major phases present in the $Al_{30}Fe_{45}Cu_{25}$ precursor alloy with different density can be visualized from the backscatter-electron SEM image (Figure 2a). However, the XRD result in Figure 2c shows only one set of peaks in $Al_{30}Fe_{45}Cu_{25}$ alloy. The diffraction pattern of the $Al_{30}Fe_{45}Cu_{25}$ alloy is similar to the diffraction pattern of BCC Fe but shifts to smaller diffraction angles, indicating larger lattice spacing. The phase diagram suggests a wide range of compositions, β−Cu−Fe-Al phase, which was divided into $\beta1+\beta2$ (Cu-rich + Fe-rich) two-phase regions.[51] After chemical dealloying of the $Al_{30}Fe_{45}Cu_{25}$ precursor alloys using 5 wt % sulfuric acid (H_2SO_4) aqueous solution at 90 °C, a bimodal structural porous Cu with both micron-sized pores and nano-sized pores was formed, as shown in Figure 2b. The dealloying process removed Fe and Al from the Cu−Fe−Al ternary alloys while the pure Cu remained, forming porous structure, as shown in the XRD pattern in Figure 2c. It was believed that the dissolution of the micron-sized Fe-rich phase forms the
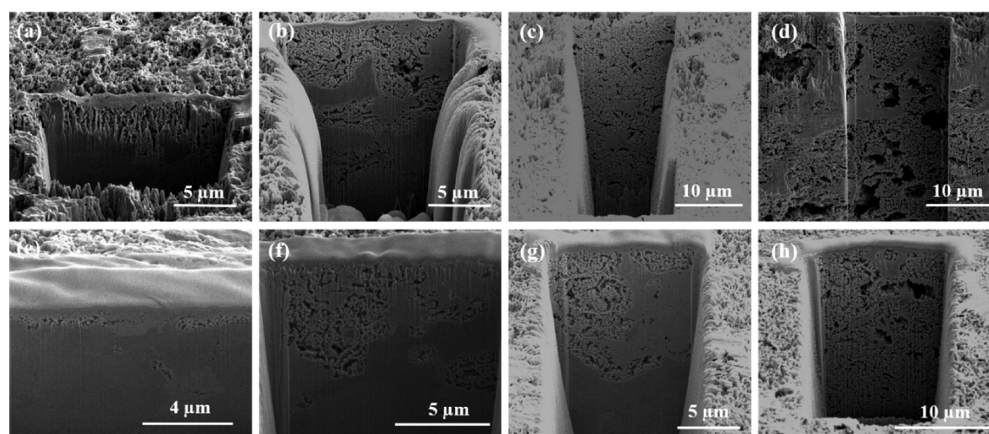
Figure 3. FIB-SEM cross-section of eight $Al_{30}Fe_{45}Cu_{25}$ precursor alloys dealloyed for different duration at different temperature. The dealloying time at 90 °C are (a) 5, (b) 10, (c) 15, and (d) 60 min. The dealloying time at 60 °C are (e) 10, (f) 30, (g) 40, and (h) 80 min.

micropores, while dealloying of Al-(Fe) from the Cu-rich phase forms the nanopores; however, the detailed temporal evolution of the materials' morphology during dealloying is to be studied, as presented below via the X-ray nano-tomography.

X-ray nano-tomography was conducted in order to investigate the morphological evolution of the Cu−Fe−Al precursor alloy and bimodal porous Cu. The 3D morphology is directly visualized as shown in the 3D volume rendering (Figure 2d−f) and 2D pseudo cross-section images (Figure 2g−j) of the $Al_{30}Fe_{45}Cu_{25}$ precursor alloy and fully dealloyed bimodal porous Cu (dealloyed for 24 h at 90 °C). After sintering, each of the Cu-rich phase and Fe-rich phase formed a three-dimensional interconnected structure each with micron-sized features, as shown in the 3D tomographic reconstruction, Figure 2d. The 2D pseudo cross sections of porous Cu are shown in Figure 2i,j. From the 2D pseudo cross sections and XRD analysis of porous Cu after fully dealloying of $Al_{30}Fe_{45}Cu_{25}$ alloy, Cu was shown to be the only remaining phase, and forms bicontinuous micron-sized pore and nano-sized pores, as shown in Figure 2e,f. Comparing panel a with panel b in Figure 2 from the SEM analysis and panels d, g, and, h with panels e, i, and j in Figure 2 from tomography analysis, the pores size of the micron-sized pore is similar to the size of the initial Fe-rich phase in the pristine alloy. The nanoporous structure in this bimodal porous Cu shows similar bicontinuous 3D morphology to other nanoporous metals which were also fabricated by chemical or electrochemical dealloying methods.[6,52−54]

3.2. Morphological Evolution and Chemical Evolution of Cu−Fe−Al Alloy during the Dealloying Process.
In order to understand the dealloying process of Cu−Fe−Al ternary alloy, $Al_{30}Fe_{45}Cu_{25}$ precursor alloy was dealloyed for different durations to investigate the morphological evolution and the progress of the reaction during dealloying by both 2D cross-sectional FIB-SEM and 3D X-ray nano-tomography. The dealloying process was conducted in 5 wt % sulfuric acid solution at both 90 and 60 °C separately to study the temperature dependence of the porous structure. The porous structure, dealloying regions, and dealloying distance can be qualitatively observed in FIB-SEM cross-section images, as shown in Figure 3. Eight $Al_{30}Fe_{45}Cu_{25}$ precursor alloys were dealloyed for different durations at 90 and 60 °C separately. At the initial stage of dealloying at 90 °C in Figure 3a, a thin layer of rough porous structure formed on the surface of precursor

alloy. With increasing dealloying time, the dealloying front progresses gradually and the dealloying distance increases, as shown in Figure 3b,c; note that during the dealloying, there were still undealloyed zones in the porous region. Moreover, only the nanoporous structure and some relative larger band-shaped pores formed during the dealloying process. Micron-sized pores appeared among the nanoporous zones until the dealloying distance propagates throughout the whole alloy. From these results, it can be found that the mechanism of bimodal porous Cu formation is a complex process. It is not as simple as nanoporous metals, and our preconception that the dealloying front propagates homogeneously from surface to center of the sample and the nanoporous structure and microporous structure are formed simultaneously, is not correct. Although the dealloying temperature will impact the dealloying speed, ligament surface morphology, and interface structure of porous metals,[55,56] the overall morphological evolution of $Al_{30}Fe_{45}Cu_{25}$ alloy dealloyed at 90 and 60 °C were consistent. However, the dealloying rate at 60 °C is slower than at 90 °C so that the dealloying process can be better controlled and quantified during the interrupted in situ experiment. Therefore, in the following section we focus on the morphology evolution of bimodal porous Cu dealloyed at 60 °C.

Because FIB-SEM is destructive so that it is not possible to investigate the morphological evolution of dealloying using the same location, the continuous 3D morphology evolution of the Cu−Fe−Al alloy was further studied by interrupted in situ X-ray nano-tomography to image a sample that has undergone repeated dealloying treatment. The experimental setup and interrupted in situ dealloying treatment for the synchrotron transmission X-ray microscopy characterization is shown in Figure 1b.

The 3D morphological evolution of $Al_{30}Fe_{45}Cu_{25}$ alloy during dealloying at 60 °C from the interrupted in situ X-ray nano-tomography is shown in Figure 4. The 3D morphological evolution of the first period (first three dealloying time points): 0 min (pristine), 10 and 30 min, showed that the dealloying first occurs in the Fe-rich phase area, where the nanoporous structure emerges. After 30 min dealloying, the Fe-rich phase has completely converted into a nanoporous structure, while the Cu-rich phase changed relatively little in comparison with the Fe-rich phase at this time point. The enlarged view provides a more detailed visualization on the 3D morphology
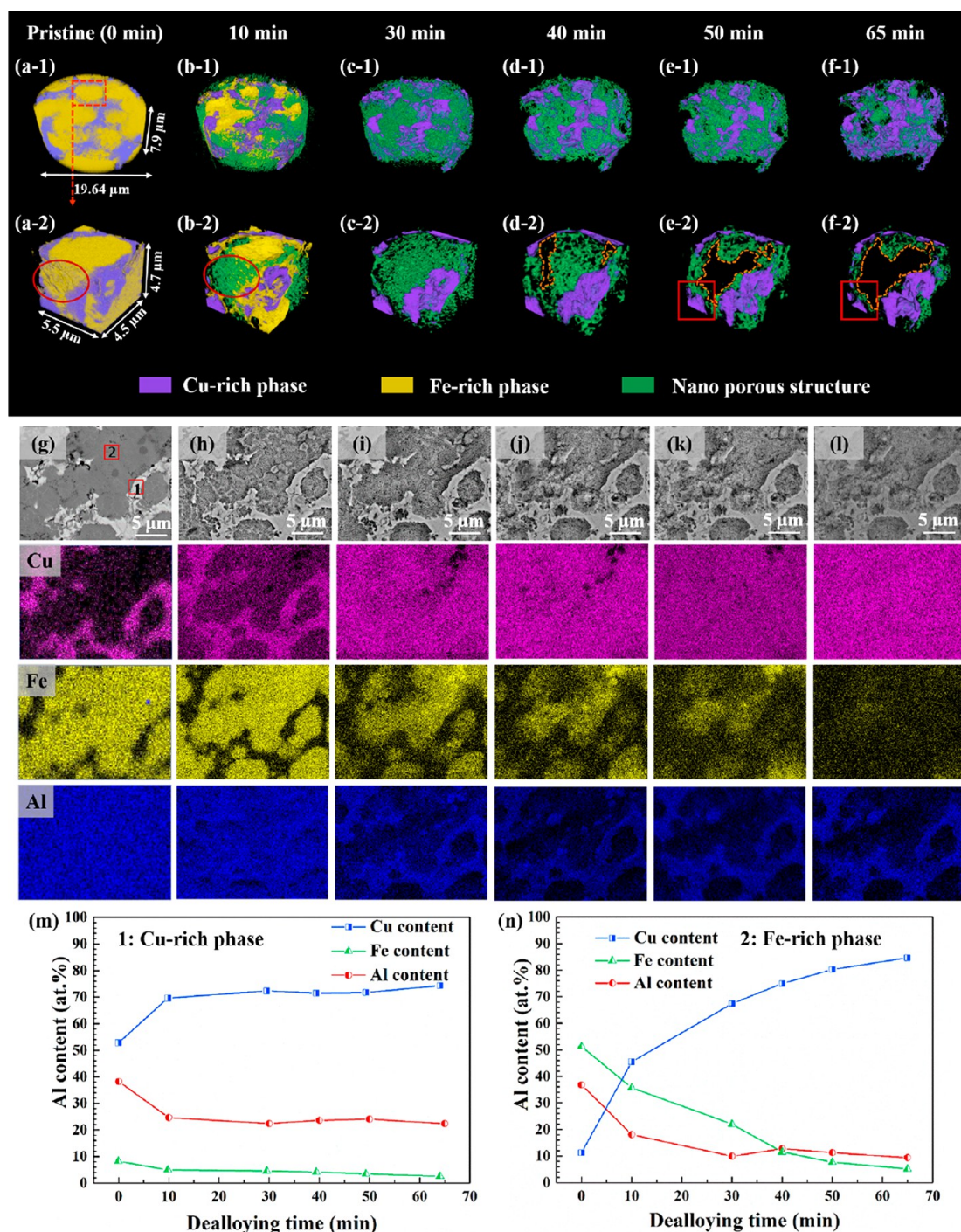
Figure 4. 3D volume rendering of X-ray nano-tomography reconstruction showing the morphological evolution of a $Al_{30}Fe_{45}Cu_{25}$ alloy sample during dealloying process from pristine to 65 min dealloying in H_2SO_4 at 60 °C. (a-1 to f-1) The 3D morphology of the imaged cylindrical sample; (a-2 to f-2) an enlarged view of 3D morphology of a region of interest cropped from a volume marked by red dash rectangle in (a-1). The red circles in (a-2) and (b-2) indicate an evolving Fe-rich region, where nanopores were developed initially, followed by a dissolution. The red rectangle in (e-2) and (f-2) indicated a Cu-rich region, where nanoporous structures were developed later. Interrupted in situ SEM-EDX of $Al_{30}Fe_{45}Cu_{25}$ alloy dealloyed at 60 °C for (g) 0, (h) 10, (i) 30, (j) 40, (k) 50, and (l) 65 min. The evolution of the relative content ratio of Cu, Fe, and Al elements: (m) Cu-rich phase marked as region 1 in (g); (n) Fe-rich phase marked as region 2 in (g).

of the samples. The area marked by red circles in Figure 4a-2 developed nanopores more rapidly than other regions, indicating that some unsintered gaps in precursor alloy would facilitate the process of dealloying by allowing the dealloying agent to diffuse within the structure.[57] This process also illustrates the possibility of forming a nanoporous Fe structure with likely iron oxides on the surface, interconnected with a conductive, micron-sized Cu support, potentially for different types of applications.

An increase in dealloying time leads to further dissolution of the initial nanoporous structure formed from the original Fe-rich phase, and the appearance of micron-sized pore, as observed in the second period (the last three dealloying time points): 40, 50, and 65 min. The micron-sized pores are
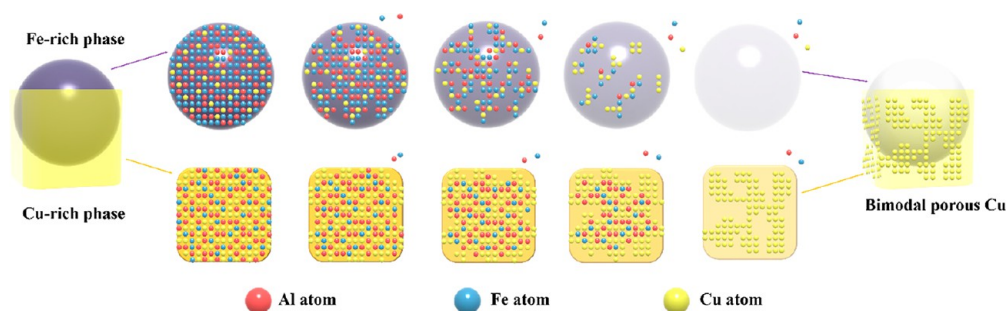
Figure 5. Schematic summarizing the mechanism of morphological evolution in the bimodal porous Cu fabricated by chemical dealloying of Cu−Fe−Al ternary alloy. The same concept can be applied to other ternary alloy systems following the design concept illustrated in Figure 1.

marked with orange dashed lines in Figure 4d-2 to f-2. It indicates that the continuous dissolution of the initial nanoporous structure has led to a gradual increase in size for the micron-sized pores with an increased dealloying time. The morphology of the Cu-rich phase starts to evolve obviously in the late stage of the second dealloying period, which can be observed by comparing the region of interest in the Cu-rich phase as marked with red rectangles in Figure 4e-2,f-2. From 50 to 65 min dealloying, the overall size of the marked Cu-rich phase decreases, and nanopores started to emerge from dealloying the Cu-rich phase. Beyond 65 min, the sample became mechanically brittle, likely due to the nanoporous structure;[58,59] continuing dealloying treatment and imaging operation processes have led to fracture and sample loss. However, through combining the 3D morphological evolution as shown here in Figure 4 and the analysis of a fully dealloyed bimodal porous Cu shown in Figure 2, it indicates that the final nanoporous structure in bimodal porous Cu is formed through further dealloying of the Cu-rich phase.

Analyzing the chemical composition evolution further clarifies the details of the dealloying process. The elemental distribution evolution of the $Al_{30}Fe_{45}Cu_{25}$ alloy during the dealloying process, measured by EDS mapping and spectra analysis, are shown in Figure 4g−n. The initial compositions of two major phases were ∼53 at. % Cu, ∼9 at. % Fe, and ∼38 at. % Al in Cu-rich phase and ∼51 at. % Fe, ∼12 at. % Cu, and ∼37 at. % Al in Fe-rich phase. After 10 min of dealloying, Fe and Al contents decrease noticeably in the Cu-rich phase; interestingly these changes did not correspond to visible morphological evolution in the X-ray nano-tomography. This is likely due to a combination of two factors: First, due to the spatial resolution of the EDS analysis in SEM, it is challenging to only detect the Cu-rich phase locally, and second, if there was morphological evolution of the Cu-rich phase at this dealloying stage, the changes might be at a length scale that were beyond the spatial resolution of the TXM. As the dealloying progresses, the relative contents of Fe, Al, and Cu remain relatively unchanged, showing 4, 23, and 73 at. % respectively. The chemical composition evolution in Fe-rich phase shows a different phenomenon: The Al content decreases significantly from 0 to 30 min, and it shows no substantial changes after that; meanwhile, the relative content of Fe continues to decrease from 51 to 5 at. % until 65 min dealloying. This is consistent with the significant morphological evolution in Fe-phase as also show in the X-ray nano-tomography analysis.

3.3. Mechanisms of Dealloying Ternary Alloy Composites.
The dealloying mechanism of the Cu−Fe−Al alloy is mainly connected with contents of active components and noble component in both Cu-rich phase and Fe-rich phase. The Fe and Al components are together considered as "active components": the SEM-EDX result showed that the contents of Fe and Al were decreasing at similar rates. Dealloying of the Cu-rich phase and the Fe-rich phase in the Cu−Fe−Al system can thus be expressed as dealloying of a $X_{50}Cu_{50}$ phase and a $X_{90}Cu_{10}$ phase (X = Fe + Al, active components), respectively. Therefore, the dealloying of Cu−Fe−Al system can be thought as a process in which a two-component composite with different contents of Cu is dealloyed to form nanoporous structure in $X_{50}Cu_{50}$ phase and to form microporous structure in $X_{90}Cu_{10}$ phase.

The elemental content in each of the alloy phase in this composite will directly impact the electrochemical activities of the phase, also known as critical potential. The higher content of noble element, the weaker electrochemical activity of phase.[26,60,61] Therefore, the $X_{90}Cu_{10}$ phase was etched more rapidly than the $X_{50}Cu_{50}$ phase. With the dissolution of active components in the $X_{90}Cu_{10}$ phase, the nanoporous structure with residual active component formed, starting from the surface first. The X content of the nanoporous structure on the surface is lower than the undissolved $X_{90}Cu_{10}$ phase inside, which leads to the decrease of electrochemical activities of the nanoporous structure. The undissolved $X_{90}Cu_{10}$ phase inside will be preferentially dealloyed. This propagation of dealloying front thus leads to a formation of nanoporous structure in the Fe-rich phase. With the increase of dealloying time, active component X in ligaments of the nanoporous structure will continue to be dissolved and the initial nanopores grow in size until all the X component is dissolved, forming a microporous structure. Note that the total content of Cu in the $X_{90}Cu_{10}$ phase is below the percolation threshold to support a continuous network structure.

At the time of the full dissolution and dealloying of the $X_{90}Cu_{10}$ phase, the dealloying of the $X_{50}Cu_{50}$ phase forms a nanoporous structure relative slowly. Therefore, after dealloying of these two phases with different Cu content, it forms a homogeneous bimodal porous structure with both nanoporosity and microporosity. Figure. 5 summarizes the schematic mechanism of the morphological evolution in this design-concept to form bimodal porous Cu.

3.4. Morphological Parameters Evolution during the Dealloying Process.
By measuring critical 3D morphological parameters, the 3D morphological evolution of bimodal porous structure during dealloying can be quantified to relate to how the dealloying process progresses. The results of quantifying the size distribution and volume fraction of the three types of features—pores, nano-ligaments, and initial Cu-rich phase—are shown in Figure 6.
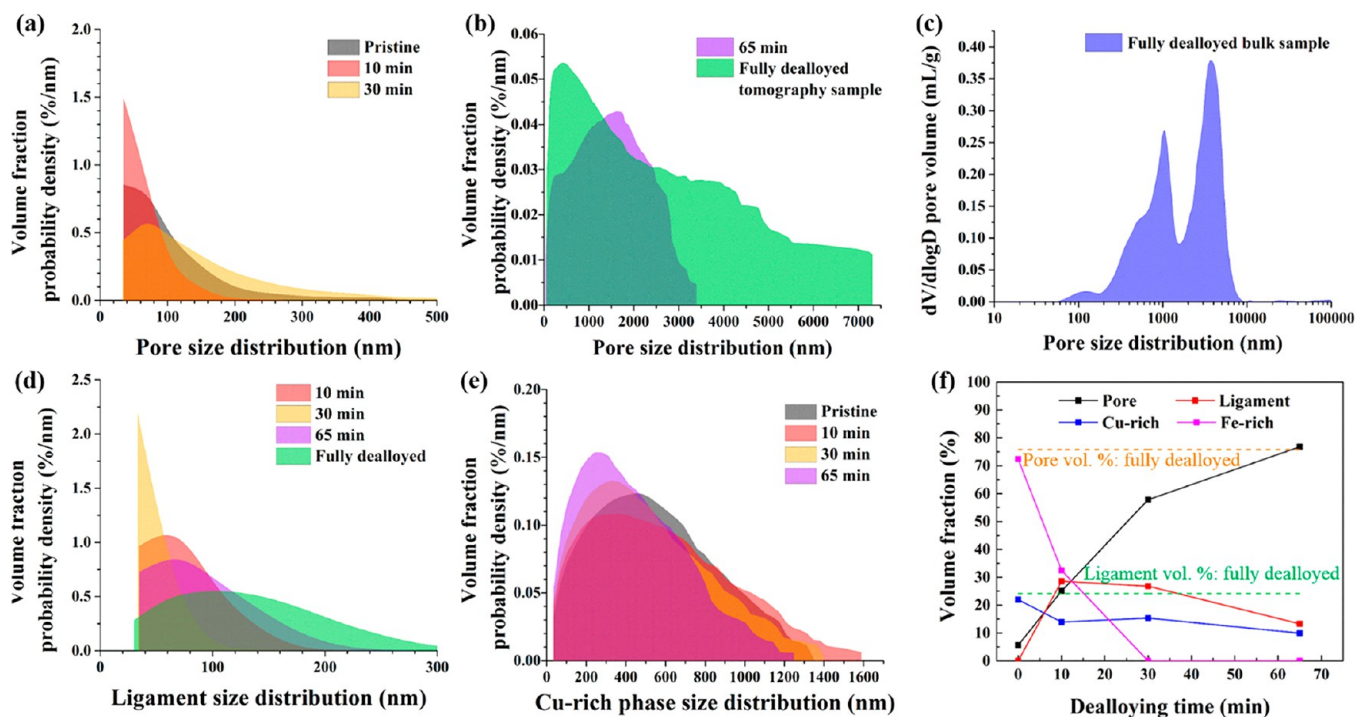
Figure 6. (a and b) Pore size distribution, quantified according to the segmented 3D images of $Al_{30}Fe_{45}Cu_{25}$ alloy dealloyed at 60 °C for 0 (pristine), 10, 30, and 65 min and fully dealloyed tomography sample; (c) pore size distribution of fully dealloyed $Al_{30}Fe_{45}Cu_{25}$ alloy bulk sample characterized using mercury porosimetry; (d) ligament size distribution and (e) Cu-rich phase size distribution of $Al_{30}Fe_{45}Cu_{25}$ alloy dealloyed at 60 °C for 0 (pristine), 10, 30, and 65 min; and (f) volume fraction of 3D morphological parameters: pores, ligaments, Cu-rich phase and Fe-rich phase. Note that the 3D morphological parameters of the sample after 40 and 50 min dealloying were not measured, because the tomographic images of these two time points appear to be out of focus during the data collection process; visualization could still be conducted on these two data sets but not quantitative calculation.

The pore size distribution result shown in Figure 6a indicates that the pore size of the sample after dealloying 10 min is smaller than the pore size of the pristine alloy. This is because the pores in the pristine alloy were from alloy preparation, while the nanopores were then formed after 10 min of dealloying. After 30 min of dealloying, although new nanoporous structures are formed due to further dealloying of the Fe-rich phase, the initial nano-ligaments formed in the Fe-rich region were also being dissolved. As a result, the ligament size after 30 min of dealloying is smaller than at 10 min, but the pore size is larger. After 65 min of dealloying, because most of the nanoporous structure formed from Fe-rich phase has been dissolved and a small amount of nanoporous structure starts to emerge in the Cu-rich phase, the ligament size at 65 min dealloying is between that at 30 min and the fully dealloyed structure. The size of Cu-rich phase does decrease significantly after 65 min of dealloying, where the morphological evolution became noticeable in the Cu-rich phase. For the fully dealloyed sample, bimodal porous structure is formed with both nano-sized pores and micron-sized pores as can be seen in Figure 6b,c.

Two important parameters, which directly impact the formation of nanoporous structure during dealloying process, are the dissolution rate of the active component(s) and the surface diffusion rate of the retained noble component(s).[62] The ligament/pore scale λ evolves depending on the balance of dissolution rate k_{diss}, which is associated with pores formation, and surface diffusion rate k_{SD}, which is associated with the aggregation of noble components into clusters, based on the following equation:[63]

$$\lambda \propto \left(\frac{k_{SD}}{k_{diss}}\right)^{1/6}$$

(1)

The choice of noble metal component directly affects the surface diffusion rate and then affects the ligament size; in general, the smaller of the diffusion rate, the smaller of the ligament size. The surface diffusion rate of Cu is faster than most of noble metals in corresponding precursor alloys alloying with the same active metal, Al,[63] leading to larger ligament size of porous Cu than other common porous noble metals, such as Pt, Pd, Au, and Ag. The size of micropores in the multiscale, bimodal porous structure mainly depends on the phase composition of Cu–Fe–Al alloy and the size of active-component-rich phase, which is Fe-rich phase in this case.

The volume fraction of Cu-rich and Fe-rich phases decrease over the course of the dealloying but occur at different stages of dealloying. The Fe-rich phase dissolves and its volume fraction reaches 0.0% after 30 min dealloying. The volume fraction of the pore phase is increasing during dealloying and the volume fraction of nano-ligament increases first and then decreases gradually because the nanoporous structure initially formed in the Fe-rich phase was dissolved gradually in the later period of the dealloying. However, the volume fraction of nano-ligament at 65 min is lower than in the fully dealloyed sample because most of the Cu-rich phase has yet to be dissolved into the nanoporous structure. After fully dealloying, the Cu-rich phase will evolve into a bicontinuous nanoporous structure consisting of nano-ligaments and nanopores, and their corresponding volume fractions change accordingly.
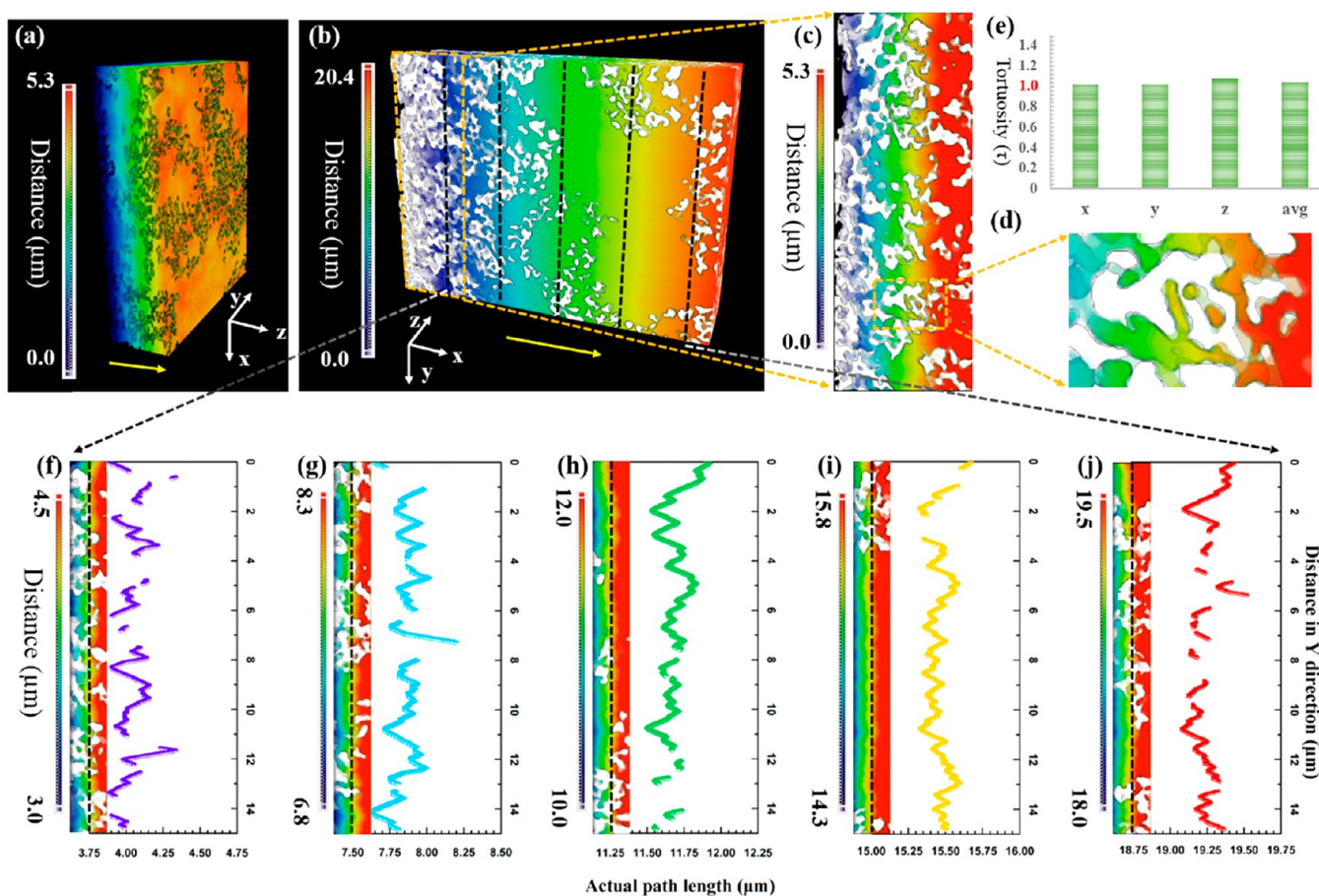
Figure 7. Tortuosity, 3D distance map, and distance profiles at a specific *x* position based on geometric propagation of bimodal porous Cu within the pore phase; white color in the structure represents the nano-ligaments. (a) Propagating along the positive *z* direction, as shown by the yellow arrow, (b) propagating along the positive *x* direction, as shown by the yellow arrow; (c and d) two levels of the enlarged view of the *x*-direction distance map, highlighting the effects of bimodal pores on transport properties; (e) tortuosity along the *x*, *y*, and *z* directions and their average value; (f-j) distance profiles showing the actual diffusion path length of bimodal porous Cu at five different *x* locations as indicated in panel b.

The 3D distance maps directly quantify and visualize the tortuosity based on geometric propagation of the fully dealloyed bimodal porous Cu as shown in Figure 7. Tortuosity, defined as the ratio between a tortuous path distance and a straight distance, is an important geometric parameter quantitatively associate the intrinsic diffusion with effective diffusivity and conductivity for porous media.[22,23,64−66] Here, the distance map is calculated within the pore phase of the structure, with the color-scale showing the actual path distance, from one side of the structure to the other side. All three orthogonal directions, each with both positive and negative propagating directions, were calculated; only the path distance maps along positive direction of *z* and *x* axes are displayed for brevity, as shown in Figure 7a,b, respectively.

The results quantitatively show that nanoporosity with small and tortuous porous structure increases the actual path length, as shown in Figure 7c,d; this can be compensated by having the microporosity which helps to maintains a more uniform propagation front to facilitate diffusion within the porous structure. The tortuosity value *τ* of bimodal porous Cu along the *x*, *y*, and *z* directions are 1.024, 1.021, and 1.073, respectively, as shown in Figure 7e. The tortuosity of nanoporous Au fabricated by electrochemical dealloying reported by Xue et al. is 3.2.[67] In comparison, the tortuosity in the liquid metal dealloyed (LMD) samples is significantly lower than that in electrochemical dealloyed samples; Zhao et

al. reported a tortuosity between 1.1 and 1.9 for porous Fe−Cr formed by LMD,[68] and the nanoporous Ti through liquid metal dealloying reported by Chen-Weigart et al. shows a tortuosity between 1.2 and 1.8.[69] The average tortuosity value 1.040 of our bimodal porous Cu is relatively low even compared with the LMD samples. The results show that the actual path length is close to the straight distance, due to the existence of microporosity; the lower tortuosity and therefore larger effectivity diffusivity may be beneficial for applications concerning transport properties. In Figure 7f−j, the distance profiles at five different *x* locations, which are marked by black dash lines in Figure 7b, visually show the actual path length of bimodal porous Cu. This provides a direct visualization on how the bimodal porous structure could be advantageous when considering both the overall transport phenomena facilitated by the microporosity, as well as the high surface area and functionaries enabled by nanoporosity.

4. CONCLUSION

In this study, bimodal porous Cu with both micron-sized pores and nano-sized pores was successfully fabricated through chemical dealloying of $Al_{30}Fe_{45}Cu_{25}$ alloy. The dealloying process of the Cu−Fe−Al alloy was systematically studied via investigating the morphological evolution during dealloying process. There are two main phases in the precursor alloy: the Cu-rich phase (∼50 at. % Cu, 40 at. % Al, and 10 at. % Fe) and

the Fe-rich phase ($\sim$50 at. % Fe, 40 at. % Al, and 10 at. % Cu). During the dealloying process, both active components Al and Fe will be dissolved at the same time until the relative content of Al reaches the critical value. At that point, the Al content remains relatively stable while Fe continues to be dissolved. By combining the analysis of 3D morphological evolution, chemical composition evolution, and quantified 3D morphological parameters evolution during dealloying process, the formation of the bimodal porous structure elucidated. The micron-sized pores are formed from dealloying of the Fe-rich phase: the first period (by 30 min), Fe-rich phase are dealloyed and form nano-sized pores with Cu-rich nano ligaments (because the dissolution of Al and Fe). During this time, there is relatively little change in the Cu-rich phase. During the second period (by 65 min), the Cu-rich nano ligaments at the area of initial Fe-rich phase (only $\sim$10 at. % of the initial Cu content in Fe-rich phase from EDX) cannot support a continuous network and, thus, break apart and/or diffuse to merge with the Cu-rich phase, leading to the formation of micron-sized pores. The formation of nano-sized pores in the final bimodal porous structure comes from simple dealloying of Cu-rich phase: the dealloying in the Cu-rich phase after about 65 min and form nanoporous structure. The overall tortuosity of the bimodal porous Cu is low because the micron-sized pores compensate for the actual path length's increase caused by nanoporosity. The 3D morphological data analysis suggests that this method allows for the precisely controlling the type of porous structure by adjusting the dealloying times. We believe that this method can also be employed in other ternary alloy systems, thereby opening the door to new technological capabilities.

■ ASSOCIATED CONTENT

ⓢ Supporting Information

The Supporting Information is available free of charge at https://pubs.acs.org/doi/10.1021/acsami.9b16392.

> Information on the importance of using X-ray nano-tomography to characterize the bimodal porous structure; comparison of different dealloying behavior in the $Cu_{25}Fe_{75}$ binary precursor alloy and the $Al_{30}Fe_{45}Cu_{25}$ ternary precursor by pseudo cross-section imaging from interrupted in situ X-ray nano-tomography conducted at below and above Cu absorption edge dealloyed at 90 °C; identifying Cu-rich phase and Fe-rich phase and their evolution by pseudo cross-section from interrupted in situ X-ray nano-tomography conducted at below and above Cu absorption edge of $Al_{30}Fe_{45}Cu_{25}$ ternary precursor alloy dealloyed at 60 °C (PDF)

> Video based on the 3D nano-tomography of Figure 2 (MP4)

> Video based on the 3D nano-tomography of Figure 4 a-1 to f-1 (MP4)

> Video based on the 3D nano-tomography of Figure 4 a-2 to f-2 (MP4)

■ AUTHOR INFORMATION

Corresponding Authors

*E-mail: sqqf@whut.edu.cn.
*E-mail: chenfei027@whut.edu.cn.
*E-mail: Karen.Chen-Wiegart@stonybrook.edu.

ORCID ⓘ

Lijie Zou: 0000-0001-9946-6537
Chonghang Zhao: 0000-0002-3538-6199
Xiaoyang Liu: 0000-0002-9326-2135
Cheng-Hung Lin: 0000-0001-9254-9751
Fei Chen: 0000-0001-9643-7191

Author Contributions

L.Z., Y.-c.K.C.-W, F.C., and Q.S. developed the research idea. L.Z. and Y.-c.K.C.-W. wrote user proposals for the use of FXI beamline at NSLS-II and equipment at CFN; H.W. prepared precursor alloy under the supervision of F.C.; L.Z. conducted dealloying and SEM/EDS analysis; L.Z. and C.Z. prepared samples for FXI beamtime. M.G., X.X., and W.L. commissioned and setup the FXI. L.Z., M.G., C.Z., Q.M., X.L., C.-H.L., X.X., W.L., and Y.-c.K.C.-W conducted the FXI experiment and preliminary data analysis during the experiment together. L.Z. conducted data analysis with inputs and guidance from M.G., C.Z., and Y.-c.K.C.-W.; Q.M. and F.C. provided scientific insights on data interpretation and mechanistic understanding. L.Z. and Y.-c.K.C.-W. wrote the manuscript, with inputs from other coauthors.

Notes

The authors declare no competing financial interest.

■ REFERENCES

(1) Shin, H. C.; Liu, M. Three-Dimensional Porous Copper-Tin Alloy Electrodes for Rechargeable Lithium Batteries. *Adv. Funct. Mater.* **2005**, *15* (4), 582−586.

(2) An, Y.; Fei, H.; Zeng, G.; Xu, X.; Ci, L.; Xi, B.; Xiong, S.; Feng, J.; Qian, Y. Vacuum Distillation Derived 3D Porous Current Collector for Stable Lithium−metal Batteries. *Nano Energy* **2018**, *47*, 503−511.

(3) Yun, Q.; He, Y. B.; Lv, W.; Zhao, Y.; Li, B.; Kang, F.; Yang, Q. H. Chemical Dealloying Derived 3D Porous Current Collector for Li Metal Anodes. *Adv. Mater.* **2016**, *28* (32), 6932−6941.

(4) Zhao, H.; Lei, D.; He, Y.-B.; Yuan, Y.; Yun, Q.; Ni, B.; Lv, W.; Li, B.; Yang, Q.-H.; Kang, F.; Lu, J. Compact 3D Copper with Uniform Porous Structure Derived by Electrochemical Dealloying as Dendrite-Free Lithium Metal Anode Current Collector. *Adv. Energy Mater.* **2018**, *8*, 1800266.

(5) Liu, Z.; Du, J.; Qiu, C.; Huang, L.; Ma, H.; Shen, D.; Ding, Y. Electrochemical Sensor for Detection of P-nitrophenol Based on Nanoporous Gold. *Electrochem. Commun.* **2009**, *11* (7), 1365−1368.

(6) Ding, Y.; Chen, M. Nanoporous Metals for Catalytic and Optical Applications. *MRS Bull.* **2009**, *34* (08), 569−576.

(7) Zhang, J.; Li, C. M. Nanoporous Metals: Fabrication Strategies and Advanced Electrochemical Applications in Catalysis, Sensing and Energy Systems. *Chem. Soc. Rev.* **2012**, *41* (21), 7016−7031.

(8) Sang, H. J.; Seong, J. C.; Ilwhan, O.; Kwak, J.; Liu, Z.; Terasaki, O.; Ryoo, R. Ordered Nanoporous Arrays of Carbon Supporting High Dispersions of Platinum Nanoparticles. *Nature* **2001**, *412*, 169−172.

(9) Lefebvre, L. P.; Banhart, J.; Dunand, D. C. Porous Metals and Metallic Foams: Current Status and Recent Developments. *Adv. Eng. Mater.* **2008**, *10* (9), 775−787.

(10) Tuchinskiy, L. Novel Manufacturing Process for Metal and Ceramic Microhoneycombs. *Adv. Eng. Mater.* **2008**, *10* (3), 219−222.

(11) Xi, Z.; Zhu, J.; Tang, H.; Ao, Q.; Zhi, H.; Wang, J.; Li, C. Progress of Application Researches of Porous Fiber Metals. *Materials* **2011**, *4* (4), 816−824.

(12) Jin, H. J.; Wang, X. L.; Parida, S.; Wang, K.; Seo, M.; Weissmuller, J. Nanoporous Au-Pt Alloys as Large Strain Electrochemical Actuators. *Nano Lett.* **2010**, *10* (1), 187−194.

(13) Shin, H. C.; Liu, M. Copper Foam Structures with Highly Porous Nanostructured Walls. *Chem. Mater.* **2004**, *16*, 5460−5464.

(14) Banhart, J. Light-Metal Foams-History of Innovation and Technological Challenges. *Adv. Eng. Mater.* **2013**, *15* (3), 82−111.

(15) Song, T.; Yan, M.; Qian, M. The Enabling Role of Dealloying in The Creation of Specific Hierarchical Porous Metal Structures—A review. *Corros. Sci.* **2018**, *134*, 78−98.

(16) Juarez, T.; Biener, J.; Weissmüller, J.; Hodge, A. M. Nanoporous Metals with Structural Hierarchy: A Review. *Adv. Eng. Mater.* **2017**, *19*, 1700389.

(17) Detsi, E.; Punzhin, S.; Rao, J.; Onck, P. R.; De Hosson, J. Th. M. Enhanced Strain in Functional Nanoporous Gold with a Dual Microscopic Length Scale Structure. *ACS Nano* **2012**, *6*, 3734−3744.

(18) Qi, Z.; Weissmuller, J. Hierarchical Nested-Network Nanostructure by Dealloying. *ACS Nano* **2013**, *7*, 5948−5954.

(19) Lu, Q.; Hutchings, G. S.; Yu, W.; Zhou, Y.; Forest, R. V.; Tao, R.; Rosen, J.; Yonemoto, B. T.; Cao, Z.; Zheng, H.; Xiao, J. Q.; Jiao, F.; Chen, J. G. Highly Porous Non-precious Bimetallic Electrocatalysts for Efficient Hydrogen Evolution. *Nat. Commun.* **2015**, *6*, 6567.

(20) Qiu, H.; Dong, X.; Huang, X. Design of Nanoporous Metals with Bimodal Pore Size Distributions for Enhanced Biosensing. *Nanoscale* **2012**, *4* (15), 4492−4497.

(21) Wada, T.; Geslin, P.-A.; Kato, H. Preparation of Hierarchical Porous Metals by Two-step Liquid Metal Dealloying. *Scr. Mater.* **2018**, *142*, 101−105.

(22) Chen-Wiegart, Y.-c. K.; DeMike, R.; Erdonmez, C.; Thornton, K.; Barnett, S. A.; Wang, J. Tortuosity Characterization of 3D Microstructure at Nano-scale for Energy Storage and Conversion Materials. *J. Power Sources* **2014**, *249*, 349−356.

(23) Li, L.; Erb, R. M.; Wang, J.; Wang, J.; Chiang, Y.-M. Fabrication of Low-Tortuosity Ultrahigh-Area-Capacity Battery Electrodes through Magnetic Alignment of Emulsion-Based Slurries. *Adv. Energy Mater.* **2019**, *9*, 1802472.

(24) Ding, Y.; Erlebacher, J. Nanoporous Metals with Controlled Multimodal Pore Size Distribution. *J. Am. Chem. Soc.* **2003**, *125*, 7772−7773.

(25) Nyce, G. W.; Hayes, R.; Hamza, A. V.; Satcher, J. H., Jr Synthesis and Characterization of Hierarchical Porous Gold Materials. *Chem. Mater.* **2007**, *19*, 344−346.

(26) Song, T.; Yan, M.; Shi, Z.; Atrens, A.; Qian, M. Creation of Bimodal Porous Copper Materials by An Annealing-Electrochemical Dealloying Approach. *Electrochim. Acta* **2015**, *164*, 288−296.

(27) Snyder, J.; Asanithi, P.; Dalton, A. B.; Erlebacher, J. Stabilized Nanoporous Metals by Dealloying Ternary Alloy Precursors. *Adv. Mater.* **2008**, *20* (24), 4883−4886.

(28) Zhang, Y.; Sun, X.; Nomura, N.; Fujita, T. Hierarchical Nanoporous Copper Architectures via 3D Printing Technique for Highly Efficient Catalysts. *Small* **2019**, *15*, 1805432.

(29) Zhu, C.; Qi, Z.; Beck, V. A.; Luneau, M.; Lattimer, J.; Chen, W.; Worsley, M. A.; Ye, J.; Duoss, E. B.; Spadaccini, C. M.; Friend, C. M.; Biener, J. Toward Digitally Controlled Catalyst Architectures: Hierarchical Nanoporous Gold via 3D Printing. *Sci. Adv.* **2018**, *4*, No. eaas9459.

(30) Takeuchi, A.; Inoue, A. Calculations of Mixing Enthaply and Mismatch Entropy for Ternary Amorphous Alloys. *Mater. Trans., JIM* **2000**, *41* (11), 1372−1378.

(31) Takeuchi, A.; Inoue, A. Classification of Bulk Metallic Glasses by Atomic Size Difference, Heat of Mixing and Period of Constituent Elements and Its Application to Characterization of The Main Alloying Element. *Mater. Trans.* **2005**, *46* (12), 2817−2829.

(32) Pham, Q. N.; Shao, B.; Kim, Y.; Won, Y. Hierarchical and Well-Ordered Porous Copper for Liquid Transport Properties Control. *ACS Appl. Mater. Interfaces* **2018**, *10* (18), 16015−16023.

(33) Luo, Z.; Xu, J.; Yuan, B.; Hu, R.; Yang, L.; Gao, Y.; Zhu, M. 3D Hierarchical Porous Cu-Based Composite Current Collector with Enhanced Ligaments for Notably Improved Cycle Stability of Sn Anode in Li-Ion Batteries. *ACS Appl. Mater. Interfaces* **2018**, *10* (26), 22050−22058.

(34) Zhang, S.; Xing, Y.; Jiang, T.; Du, Z.; Li, F.; He, L.; Liu, W. A Three-dimensional Tin-coated Nanoporous Copper for Lithium-ion Battery Anodes. *J. Power Sources* **2011**, *196* (16), 6915−6919.

(35) Song, R.; Zhang, L.; Zhu, F.; Li, W.; Fu, Z.; Chen, B.; Chen, M.; Zeng, H.; Pan, D. Hierarchical Nanoporous Copper Fabricated by One-Step Dealloying Toward Ultrasensitive Surface-Enhanced Raman Sensing. *Adv. Mater. Interfaces* **2018**, *5*, 800332.

(36) Zhang, H.; Pan, Q.; Zhang, H. Multi-scale Porous Copper Foams as Wick Structures. *Mater. Lett.* **2013**, *106*, 360−362.

(37) Wang, S.; Zhang, Y.; Schuman, C.; Lecomte, J.-S.; Zhao, X.; Zuo, L.; Philippe, M.-J.; Esling, C. Study of Twinning/Detwinning Behaviors of Ti by Interrupted in situ Tensile Tests. *Acta Mater.* **2015**, *82*, 424−436.

(38) Zou, N.; Li, Z.; Zhang, Y.; Gan, W.; Yang, B.; Zhao, X.; Esling, C.; Hofmann, M.; Zuo, L. Deformation of Ni−Mn-Ga 7M Modulated Martensite Through Detwinning/Twinning and Forward/Reverse Intermartensitic Transformation Studied by In-situ Neutron Diffraction and Interrupted In-situ EBSD. *Acta Mater.* **2019**, *174*, 319−331.

(39) Bouttes, D.; Gouillart, E.; Boller, E.; Dalmas, D.; Vandembroucq, D. Fragmentation and Limits to Dynamical Scaling in Viscous Coarsening: an Interrupted in situ X-ray Tomographic Study. *Phys. Rev. Lett.* **2014**, *112*, 245701.

(40) Ye, X. X.; Imai, H.; Shen, J. H.; Chen, B.; Han, G. Q.; Umeda, J.; Takahashi, M.; Kondoh, K. Strengthening-toughening Mechanism Study of Powder Metallurgy Ti-Si Alloy by Interrupted In-situ Tensile Tests. *J. Alloys Compd.* **2017**, *694*, 82−92.

(41) Chen-Wiegart, Y. C.; Camino, F. E.; Wang, J. Sample Preparation of Energy Materials for X-ray Nanotomography with Micromanipulation. *ChemPhysChem* **2014**, *15* (8), 1587−1591.

(42) Kennouche, D.; Chen-Wiegart, Y.-c. K.; Yakal-Kremski, K. J.; Wang, J.; Gibbs, J. W.; Voorhees, P. W.; Barnett, S. A. Observing the Microstructural Evolution of Ni-Yttria-stabilized Zirconia Solid Oxide Fuel Cell Anodes. *Acta Mater.* **2016**, *103*, 204−210.

(43) Zernike, F. How I Discovered Phase Contrast. *Science* **1955**, *121*, 345−349.

(44) Chen-Wiegart, Y.-c. K.; Wang, S.; Lee, W.-K.; McNulty, I.; Voorhees, P. W.; Dunand, D. C. In situ Imaging of Dealloying During Nanoporous Gold Formation by Transmission X-ray Microscopy. *Acta Mater.* **2013**, *61* (4), 1118−1125.

(45) Ge, M.; Coburn, D. S.; Nazaretski, E.; Xu, W.; Gofron, K.; Xu, H.; Yin, Z.; Lee, W.-K. One-minute Nano-tomography Using Hard X-ray Full-field Transmission Microscope. *Appl. Phys. Lett.* **2018**, *113*, No. 083109.

(46) Gursoy, D.; De Carlo, F.; Xiao, X.; Jacobsen, C. TomoPy: A Framework for The Analysis of Synchrotron Tomographic Data. *J. Synchrotron Radiat.* **2014**, *21*, 1188−1193.

(47) O'Mara, A.; King, A. E.; Vickers, J. C.; Kirkcaldie, M. T. K. ImageSURF: An ImageJ Plugin for Batch Pixel-Based Image Segmentation Using Random Forests. *Journal of Open Research Software* **2017**, *5*, 31.

(48) Collins, J. M.; King, A. E.; Woodhouse, A.; Kirkcaldie, M.; Vickers, J. Age Moderates the Effects of Traumatic Brain Injury on Beta-amyloid Plaque Load in APP/PS1Mice. *J. Neurotrauma* **2019**, *36*, 1−14.

(49) Münch, B.; Holzer, L. Contradicting Geometrical Concepts in Pore Size Analysis Attained with Electron Microscopy and Mercury Intrusion. *J. Am. Ceram. Soc.* **2008**, *91* (12), 4059−4067.

(50) Zou, L.; Chen, F.; Wang, H.; Shen, Q.; Lavernia, E. J.; Zhang, L. Influence of Porosity on Mechanical Behavior of Porous Cu Fabricated via De-Alloying of Cu−Fe Alloy. *Met. Mater. Int.* **2019**, *25* (1), 83−93.

(51) Wang, C. P.; Zhang, L.; Ishida, K. *Aluminium − Copper − Iron*; Landolt-Börnstein - Group IV Physical Chemistry, 2005; Vol. *11A2*.

(52) McCue, I.; Benn, E.; Gaskey, B.; Erlebacher, J. Dealloying and Dealloyed Materials. *Annu. Rev. Mater. Res.* **2016**, *46* (1), 263−286.

(53) Zhang, C.; Sun, J.; Xu, J.; Wang, X.; Ji, H.; Zhao, C.; Zhang, Z. Formation and Microstructure of Nanoporous Silver by Dealloying Rapidly Solidified Zn−Ag Alloys. *Electrochim. Acta* **2012**, *63*, 302−311.

(54) Qi, Z.; Zhao, C.; Wang, X.; Lin, J.; Shao, W.; Zhang, Z.; Bian, X. Formation and Characterization of Monolithic Nanoporous Copper by Chemical Dealloying of Al-Cu Alloys. *J. Phys. Chem. C* **2009**, *113*, 6694−6698.

(55) Liu, T.; Zhu, M.; Shen, H.; Qin, C.; Cao, Y. The Influences of Dealloying Temperature and Time on the Morphology, Structure, and Magnetic Properties of Porous Co Nanoparticles. *J. Nanopart. Res.* **2013**, *15*, 1476.

(56) Liu, W.; Cheng, P.; Yan, J.; Li, N.; Shi, S.; Zhang, S. Temperature-induced Surface Reconstruction and Interface Structure Evolution on Ligament of Nanoporous Copper. *Sci. Rep.* **2018**, *8*, 447.

(57) Shaikh, F. U. A. Effect of Cracking on Corrosion of Steel in Concrete. *Int. J. Concr. Struct. Mater.* **2018**, *12*, 0234 DOI: 10.1186/s40069-018-0234-y.

(58) Jiao, J.; Huber, N. Deformation Mechanisms in Nanoporous Metals: Effect of Ligament Shape and Disorder. *Comput. Mater. Sci.* **2017**, *127*, 194−203.

(59) Farkas, D.; Caro, A.; Bringa, E.; Crowson, D. Mechanical Response of Nanoporous Gold. *Acta Mater.* **2013**, *61* (9), 3249−3256.

(60) Zhang, Q.; Zhang, Z. On the Electrochemical Dealloying of Al-based Alloys in a NaCl Aqueous Solution. *Phys. Chem. Chem. Phys.* **2010**, *12* (7), 1453−1472.

(61) Li, J.; Yang, Z.; Wang, T.; Yu, N.; Sun, L.; Nie, C.; Teng, H.; Jin, C.; Chen, X.; Geng, H. Tailored Products of Dealloying As-

sintered Al−Cu Alloys in Sodium Hydroxide Solutions. *RSC Adv.* **2015**, *5* (92), 75044−75054.

(62) Zhu, C.; Du, D.; Eychmuller, A.; Lin, Y. Engineering Ordered and Nonordered Porous Noble Metal Nanostructures: Synthesis, Assembly, and Their Applications in Electrochemistry. *Chem. Rev.* **2015**, *115* (16), 8896−8943.

(63) Kloke, A.; Stetten, F.; Zengerle, R.; Kerzenmacher, S. Strategies for the Fabrication of Porous Platinum Electrodes. *Adv. Mater.* **2011**, *23* (43), 4976−5008.

(64) Bae, C. J.; Erdonmez, C. K.; Halloran, J. W.; Chiang, Y. M. Design of Battery Electrodes with Dual-scale Porosity to Minimize Tortuosity and Maximize Performance. *Adv. Mater.* **2013**, *25* (9), 1254−1258.

(65) Tjaden, B.; Brett, D. J. L.; Shearing, P. R. Tortuosity in Electrochemical Devices: A Review of Calculation Approaches. *Int. Mater. Rev.* **2018**, *63* (2), 47−67.

(66) Delattre, B.; Amin, R.; Sander, J.; De Coninck, J.; Tomsia, A. P.; Chiang, Y.-M. Impact of Pore Tortuosity on Electrode Kinetics in Lithium Battery Electrodes: Study in Directionally Freeze-Cast LiNi0.8Co0.15Al0.05O2(NCA). *J. Electrochem. Soc.* **2018**, *165* (2), A388−A395.

(67) Xue, Y.; Markmann, J.; Duan, H.; Weissmuller, J.; Huber, P. Switchable Imbibition in Nanoporous Gold. *Nat. Commun.* **2014**, *5*, 4237.

(68) Zhao, C.; Wada, T.; De Andrade, V.; Williams, G. J.; Gelb, J.; Li, L.; Thieme, J.; Kato, H.; Chen-Wiegart, Y. K. Three-Dimensional Morphological and Chemical Evolution of Nanoporous Stainless Steel by Liquid Metal Dealloying. *ACS Appl. Mater. Interfaces* **2017**, *9* (39), 34172−34184.

(69) Chen-Wiegart, Y.-c. K.; Wada, T.; Butakov, N.; Xiao, X.; De Carlo, F.; Kato, H.; Wang, J.; Dunand, D. C.; Maire, E. 3D Morphological Evolution of Porous Titanium by X-ray Micro- and Nano-tomography. *J. Mater. Res.* **2013**, *28* (17), 2444−2452.